Delft University of Technology

A Flexure-Based Linear Guide With Torsion Reinforcement Structures

Rommers, J.; Naves, M.; Brouwer, D. M.; Herder, J. L.

Important note
To cite this publication, please use the final published version (if applicable).
Please check the document version above.

J. Rommers

Department of Precision and Microsystems
Engineering,
Delft University of Technology,
Delft 2628 CD, The Netherlands
e-mail: J.Rommers@tudelft.nl

M. Naves

Chair of Precision Engineering,
University of Twente,
P. O. Box 217,
7500AE Enschede, The Netherlands
e-mail: M.Naves@utwente.nl

D. M. Brouwer

Chair of Precision Engineering,
University of Twente,
P. O. Box 217,
7500AE Enschede, The Netherlands
e-mail: D.M.Brouwer@utwente.nl

J. L. Herder

Department of Precision and Microsystems
Engineering,
Delft University of Technology,
Delft 2628 CD, The Netherlands
e-mail: J.L.Herder@tudelft.nl

A Flexure-Based Linear Guide With Torsion Reinforcement Structures

In this study, a flexure-based (compliant) linear guide with a motion range comparable to its footprint is presented. The design consists of two-folded leaf springs on which torsion reinforcement structures are added. Due to these structures, only two-folded leaf springs are needed instead of a minimum of five as in preexisting designs. The new design is compared to such a preexisting design, after optimizing both on a support stiffness metric. The new design scores over twice as high on the support stiffness metric, while occupying a smaller (−33%) and a less obstructive build volume. Stress, build volume, and manufacturing limitations are taken into account. In addition, a variation on the new design using three torsion reinforced folded leaf springs is presented and optimized. This design occupies a build volume similar to the preexisting design, but scores four times higher on the support stiffness metric. A prototype of the new design is built and its parasitic eigenfrequencies are measured, validating the theoretical models (normalized mean absolute error of 4.3%). [DOI: 10.1115/1.4052971]

Keywords: compliant mechanisms, dynamics, mechanism design, mechanism synthesis, robot design

1 Introduction

Unlike rigid-body mechanisms that gain their mobility through rolling or sliding contacts, flexure (or compliant) mechanisms use the elastic deformation of slender segments to enable motion. The inherent absence of friction and play makes these mechanisms particularly suitable for precision positioning applications due to their excellent repeatability [1–7]. This study focuses on flexure-based linear guides, which allow a single translational motion of the end effector along a straight line.

The majority of the linear guide designs in literature are planar, meaning that they are fabricated monolithically from a single plate. The simplest design is composed of two leaf springs and a rigid body in a parallelogram configuration [8]. This design suffers from parasitic motions, which can be mitigated by nesting two parallelograms [9]. However, this results in an unconstrained intermediate body, which decreases both the static and dynamic performances [2,10,11]. Efforts to solve this problem include a design in which the intermediate body is coupled to the main stage by means of a lever system [8,12], one where the intermediate bodies of two double parallelogram building blocks are connected [13], and a constraining mechanism cleverly nested inside the parallelogram [10]. Not all designs in the literature are based on the parallelogram. Examples are a design based on the Robert's mechanism [14] and the Watt's mechanism [12,15].

Some spatial linear guides are described in the literature. These designs generally have larger motion ranges compared to the planar designs because self-collisions can be avoided. The two main designs are based on diaphragm flexures [16–18] and folded leaf springs [8,18–21]. The diaphragm design has a low-cost potential but suffers from a trade-off between parasitic rotation and range of motion [17]. The linear guide consisting of six-folded leaf spring (6-FLS) is shown in Fig. 1. The 6-FLS design is highly suitable for

large ranges, but its protruding elements result in an obstructive build volume. This is because at least five-folded leaf springs are necessary to constrain five degrees-of-freedom of its end effector, as will be explained in more detail in Sec. 2.1. The design is mostly known in industry and has not been described extensively in the literature [8,18–21].

In this study, we present a new linear guide with a motion range comparable to its footprint. The design consists of two-folded leaf springs on which torsion reinforcement structures are added: torsion reinforced folded leaf springs (TR-FLS). Due to the
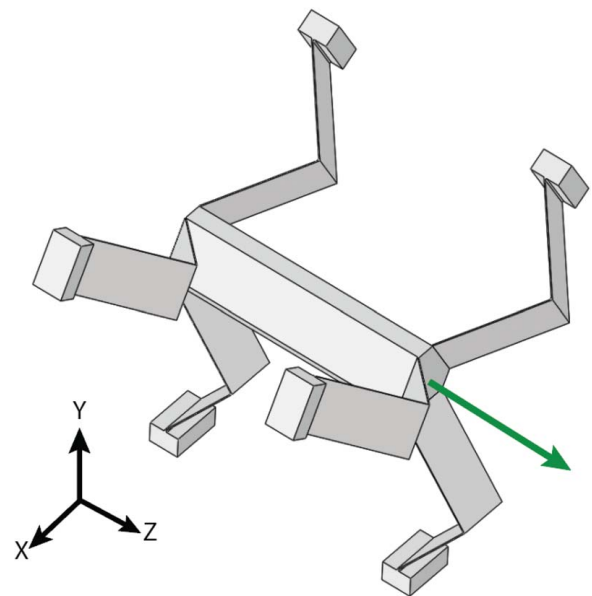
Fig. 1   The preexisting 6-FLS linear guide, which needs at least five FLS elements to constrain the five motions, leading to a large and obstructive build volume

reinforcements, only two elements are needed rather than five or six as in preexisting designs. This results in a smaller and less obstructive build volume than the preexisting 6-FLS design shown in Fig. 1. We call the new design the 2-TR-FLS. We will optimize and compare the 2-TR-FLS and the 6-FLS design, focusing on support stiffness (also known as *off-axis stiffness*) and build volume. Limits on stress and manufacturing techniques are taken into account. In addition, we present a variation on the new design called the 3-TR-FLS, which has a build volume comparable to the 6-FLS design. This design will be optimized and compared in the same manner.

Section 2 presents the three linear guides. Section 3 explains the optimization and comparison procedure. Section 4 presents an experimental validation of the theoretical models, using a prototype based on the optimized 2-TR-FLS design. We reflect on the results in the Sec. 5 and summarize the contributions to literature in Sec. 6.

2 Linear Guide Designs

In this section, first, the working principle of the preexisting 6-FLS design will be described. Then, the torsion reinforced folded leaf spring (TR-FLS) will be explained. Subsequently, the two new linear guides composed of this element are presented.

2.1 The Six-Folded Leaf Spring Linear Guide. Figure 2 shows one of the FLS of the 6-FLS guide illustrated in Fig. 1. The FLS is fixed at the left side and the block at the right side represents its end effector e. The lower part of Fig. 2 shows a rigid-body model, in which the deformation modes with low stiffness are visualized using revolute joints [9]. Bending of the leaf springs is represented by the vertical revolute joints, and torsional deformation is represented by a revolute joint coincident with the length axis of the flexures. The end effector e is extended to reach the point underneath the fold line, at which the arrow engages. At this point, motion in z-direction is not possible in the kinematic model, meaning that it is constrained in the real FLS. This is only true for a point on the indicated dashed line running through the fold line [8,22]. Rotations of the end effector are free because the revolute joints span the full space. This means that the FLS only constrains one translation. A FLS could be replaced by a wire flexure (essentially a slender rod) placed at the fold line without changing the kinematics of the mechanism [8,22,23]. The advantage of a FLS over a wire flexure is that it does not suffer from a shortening effect, which makes it specifically suitable for large ranges of motion.

Because a single FLS constrains only one degree-of-freedom of its end effector, at least five FLS elements are needed to create a linear guide. A sixth FLS is usually added to improve symmetry.

In pseudo-rigid body models [1], a blade flexure is often represented without the revolute joint that represents torsion. This representation is valid for planar mechanisms with planar loads, but if spatial loads are present, the torsional compliance needs to be taken into account [23,24]. To illustrate this, consider a typical blade flexure with length $L = 100$ mm, height (in x-direction in Fig. 2) $h = 20$ mm, thickness $t = 0.2$ mm, $E = 210$ GPa, and $G = 80$ GPa. The torsional stiffness is expressed as follows [25]:

$$K_T = \frac{GJ}{L} \quad (1)$$

where $J = \frac{1}{3} ht^3$ for wide cross sections [25]. The bending stiffness (rotation around the x-direction in Fig. 2) is expressed as follows [26]:

$$K_{rx} = \frac{EI_{rx}}{L} \quad (2)$$

where the area moment of inertia around the x-axis is $I_{rx} = \frac{1}{12} ht^3$. The in-plane bending stiffness of the blade flexure (around the axis perpendicular to the x-axis and the torsion axis) is expressed as follows:

$$K_{ipb} = \frac{EI_{ipb}}{L} \quad (3)$$

where $I_{ipb} = \frac{1}{12} th^3$. For the chosen dimensions, this results in the stiffness values $K_T = 4.3 \times 10^{-2}$ Nm/rad, $K_{rx} = 2.8 \times 10^{-2}$ Nm/rad, and $K_{ipb} = 2.8 \times 10^2$ Nm/rad. The torsion stiffness K_T has the same order of magnitude as stiffness K_{rx}, which are both indeed considered as free in the kinematic model. The in-plane bending stiffness K_{ipb} is four orders of magnitude higher and is considered as constrained in the kinematic model. The low torsional stiffness of the blade flexures is the reason that the FLS only provides a translation stiffness at point c in the X-direction. For example, the stiffness in x-direction at the end effector e due to the torsional stiffness of the left blade flexure is (assuming for simplicity that the two blades are at an angle of 90 deg) expressed as follows:
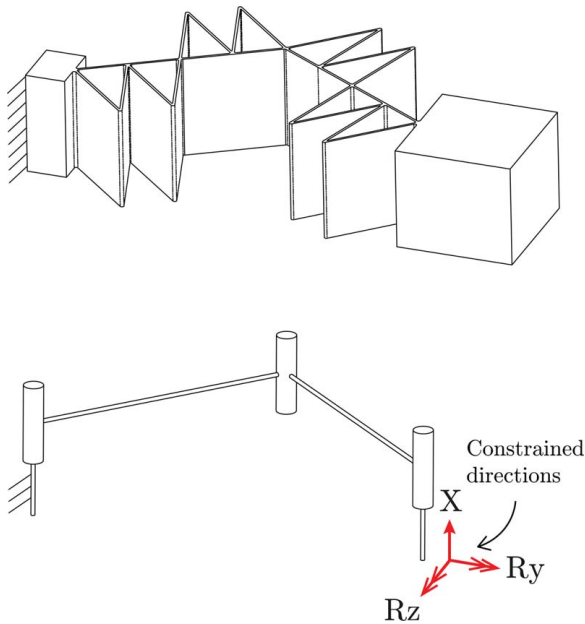
$$K_{xe,T} = \frac{K_T}{l^2} \quad (4)$$

Note that the total stiffness at point e is actually lower because not all deformations are taken into account. The stiffness at c in the x-direction is not dependent on the torsional stiffness, but on the lateral stiffness of the two blade flexures, as follows [8]:

$$K_{xc} = \left[\frac{2L^3}{3EI_{ipb}} + \frac{12L}{5Gth} \right]^{-1} \quad (5)$$

For the chosen blade flexure dimensions, stiffness $K_{xc} = 4.1 \times 10^4$ N/m and $K_{xe,T} = 4.3$ N/m. The stiffness at point c is at least four orders of magnitude higher than the stiffness at point e, which validates that the FLS provides a constraint at c and not at e. For blade flexures with a smaller length-to-height ratio, additional stiffness due to constrained warping has to be taken into account when computing the torsion stiffness in Eq. (1) [27]. However, this effect is small compared to the difference in free and constrained stiffness terms [27].
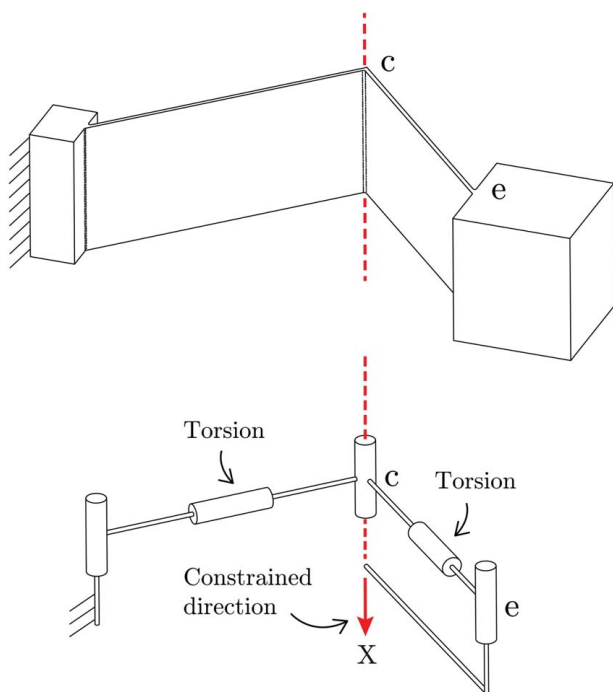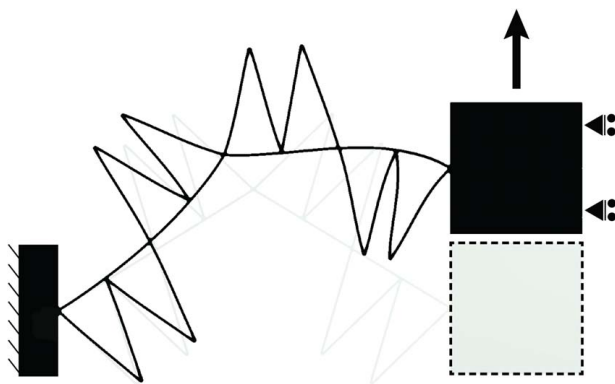

Fig. 2 The folded leaf spring (FLS) and its rigid-body model. The arrow shows its single translational constraint.
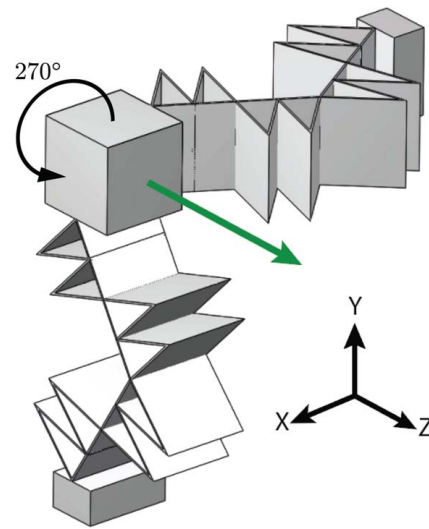
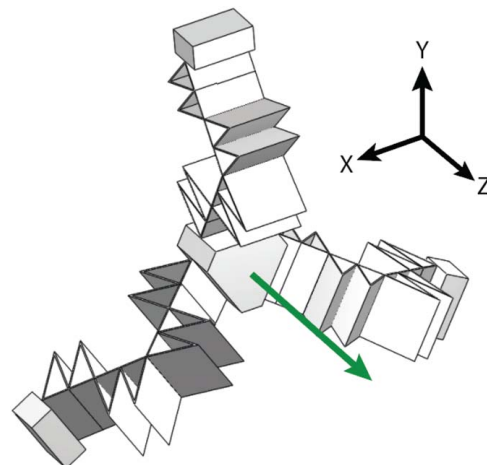Fig. 3 The TR-FLS element and its rigid-body model, showing the three constrained directions

Fig. 5 2-TR-FLS linear guide, showing a smaller and less obstructive build volume than the 6-FLS design. The end effector can be reached through a 270 deg angle.

2.2 The Torsion Reinforced Folded Leaf Spring. Figure 3 shows the TR-FLS element, consisting of a folded leaf spring with torsion reinforcement structures. These structures are proposed in earlier work [27,28], in which they are used to create a flexure joint with high stiffness in its supporting directions, at large rotations. Instead, we will use the torsion reinforcement structures to add two rotational constraints to the FLS. The lower part of Fig. 3 shows this using a rigid-body model of the TR-FLS. The two revolute joints representing torsion in Fig. 2 are now removed, resulting in a planar linkage. Note that the torsion reinforcement structures suppress torsion of the two separate blade flexures. This in turn results in different degrees-of-freedom of the end effector in the complete TR-FLS. The TR-FLS only allows movements in the XY-plane: translation in Z and rotation around X and Y are constrained. Furthermore, the TR-FLS constrains motion in z-direction at any place, contrarily to the FLS in which the motion is only constrained for points on the line running through the fold line.

It is important to note that the torsion reinforcement structures in the TR-FLS are not rigid, but behave as leaf springs. This results in a smooth strain distribution, as visualized in Fig. 4. If the torsion reinforcement structures would be rigid (as in, for example, Ref. [29]), all strains would be localized between the triangular shapes, which would lead to high peaks in the distribution.

2.3 The 2-TR-FLS Linear Guide. Figure 5 shows the 2-TR-FLS linear guide. As shown in Fig. 3, a single TR-FLS only allows in-plane motions. The intersection of the motion planes of the two TR-FLS elements forms a line, over which the end effector of the linear guide moves. This is similar to the well-known rigid link Sarrus mechanism. The 2-TR-FLS has a less obstructive build volume than the 6-FLS guide shown in Fig. 1. The end effector is accessible through a 270 deg angle. Note that the two TR-FLS elements do not necessarily have to be at a 90 deg angle, as long as the two motion planes are not parallel. Similar to the Sarrus (and the 6-FLS) mechanism, the rotation around the Z axis of the 2-TR-FLS is *overconstrained*. This is discussed in Sec. 5.

2.4 3-TR-FLS Linear Guide. Figure 6 shows the 3-TR-FLS linear guide, constructed by adding a third TR-FLS element to the 2-TR-FLS design. The motion plane of this third TR-FLS element again intersects at the motion axis. This design is mainly

Fig. 4 Visualization of the deformations in the TR-FLS (scale 1:1). Note that the triangular shapes consist of blade flexures, resulting in distributed strains. The flexure thickness in the figure is equal for all parts.

Fig. 6 3-TR-FLS linear guide for comparison purposes

considered for comparative purposes because the 6-FLS can be constructed such that it has the same build volume as the 3-TR-FLS design. This is explained Sec. 3.

3 Optimization and Comparison

The 2-TR-FLS, 3-TR-FLS, and 6-FLS designs will be optimized for a high support (or *off-axis*) stiffness, which is scored using a single performance metric. The designs are subjected to the same optimization constraints such as build volume and maximum stress. The optimization will be carried out using the flexible multibody software SPACAR [30]. In the following, first the performance metric will be defined more precisely. Then, the optimization variables, constraints, and algorithm are described, and finally, the results are presented.

3.1 Performance Metric. All three linear guides are optimized for high support stiffness, which will be scored using a single performance metric (or *optimization criterion*). The support stiffness is defined as the lowest stiffness of the end effector in any direction in the XY-plane. The support stiffness typically varies when the end effector is at a different Z-position. Therefore, the lowest support stiffness during motion in Z is used to score the designs. Another way of explaining the performance metric is that it is the lowest off-axis stiffness experienced anywhere in the motion range.

This particular performance metric is chosen because the lowest parasitic eigenfrequency (belonging to a mode shape in an undesired direction of the end effector) of the linear guide is anticipated to correspond to a translational mode shape, thus determining the dynamic behavior of the mechanism. A translational mode shape is expected because the end effector is small compared to the flexures and therefore has a relatively low rotational inertia compared to its mass.

3.2 Optimization Variables and Constraints. Figure 7 shows the design variables that are varied in the optimization routine. p depicts the point in which the support stiffness is determined and at which the mechanism is actuated. The y-coordinate of this point has the fixed value W_{end} and the variable L_{end} is the distance between this point and the attachment of the flexure. The variable θ is introduced to allow the design to rotate with respect to its motion path. Variables t_t and t_{ff} depict the thickness of the flexures of the torsion reinforcement and the folded leaf spring itself, respectively. The height of the flexures in the third dimension is not drawn and is named H. L_{ff}, W_{ff}, and W_t are the distance between the two attachment points of the flexure, the width of the main flexure, and the width of the torsion reinforcement structures, respectively. Note that the 6-FLS design only contains part of the variables depicted in Fig. 7. A spacing of 75 mm between the leaf springs of the 6-FLS design is chosen. This way, the footprint measure as depicted in Fig. 8 will approximate those of the other mechanisms, allowing for a fair comparison. Tables 1 and 2 show the constraints and the fixed values used in the optimizations, respectively. A maximum of 50 mm for the height H of the flexures is chosen because the cross-section of the end effector measures 50 by 50 mm.

3.3 Optimization Algorithm. A derivative-free function comparison search method based on the Nelder–Mead optimization algorithm [31] is used to find the set of design variables for each of the three linear guide designs, which scores highest on the performance metric defined in Sec. 3.1. To include all constraints from Table 1, the algorithm is adapted to ensure feasible solutions within the solution space as in earlier work of two of the authors [28]. The performance metric is computed using the flexible multibody software SPACAR [30]. SPACAR uses nonlinear 3D finite beam elements, which include geometric nonlinearities. Due to the specific choice of discrete deformation modes, only a limited number of
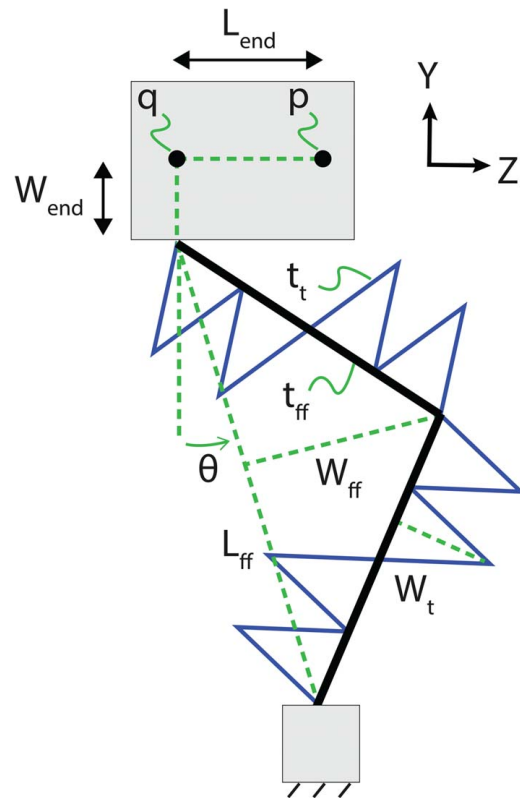

Fig. 7 Design variables of the TR-FLS. p depicts the point in which the stiffnesses are determined. The height of the flexures in the third dimension is not drawn and is named *H*. Variables *t_t* and *t_ff* depict the thickness of the torsion reinforcement structure and the folded leaf spring itself, respectively.

elements is required to produce both fast and accurate results. Computational cost is further reduced by taking into account symmetry conditions of the full mechanisms.

3.4 Optimization Results. Figure 9 shows the support stiffness of the three optimized linear guides along their motion range. Note that the following figures are semi-log plots. Support stiffness was defined as the lowest translational stiffness in the XY-plane. The minimum support stiffness in the motion range is presented in Table 3. Note that this was the performance metric in the optimization.

Figures 10 and 11 show the stiffness of the optimized linear guides in other directions. Note that the designs are not optimized on these measures. Figure 10 shows the rotational support stiffness, defined as the lowest rotational stiffness in the XY-plane. Figure 11 shows the torsional stiffness around the motion axis Z.
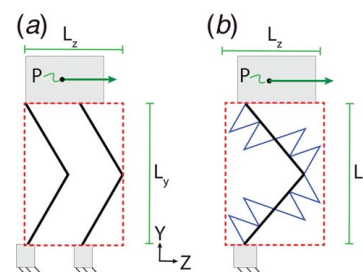

Fig. 8 Footprint measures for (*a*) the 6-FLS design and (*b*) the 2-TR-FLS and 3-TR-FLS linear guides. The 2-TR-FLS design uses only two of these blocks, whereas the other two designs need three blocks.

Table 1 Optimization constraints, depicted in Fig. 7

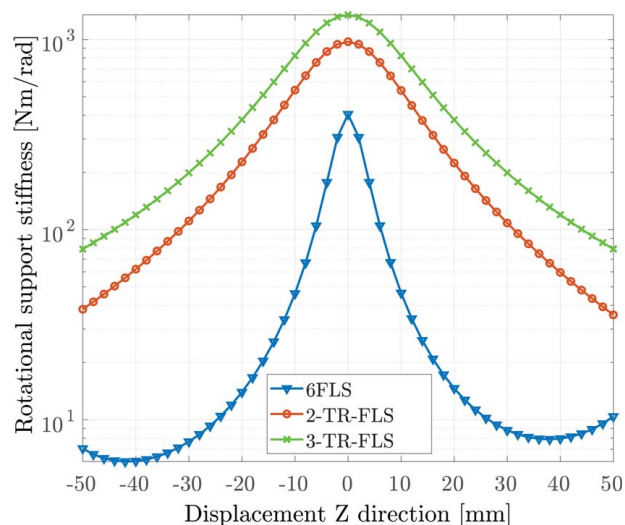| Constraint	Value
Maximum stress (Mpa)	600
Minimum flexure thickness t_{ff} and t_{tr} (mm)	0.2
Maximum flexure height H (mm)	50
Maximum Y dimension L_Y (mm)	150
Maximum driving force (N)	10
No collisions	—

Table 2 Fixed parameters in the optimizations, depicted in Fig. 7

Fixed parameter	Value
Motion range in z-direction (mm)	−50 to +50
End effector W_{end} (mm)	25
E modulus (GPa)	210
Poisson ratio (–)	0.3125
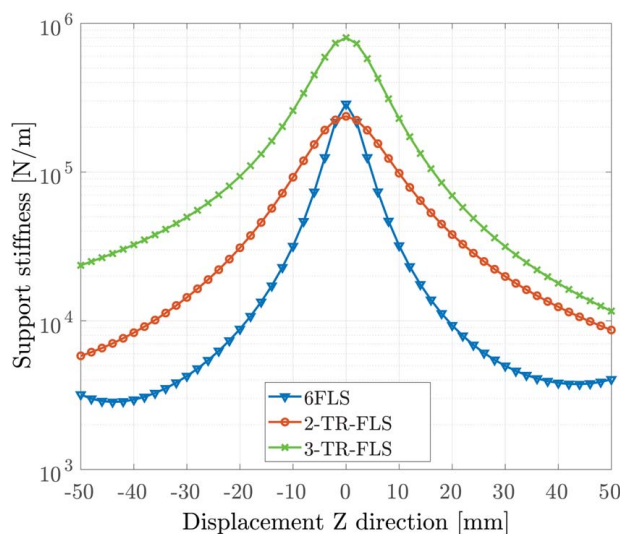
Fig. 10 Rotational support stiffness versus displacement of the three optimized designs, defined as the lowest rotational stiffness vector in the XY-plane

Fig. 9 Support stiffness versus displacement of the three optimized designs, defined as the lowest translational stiffness in the XY-plane
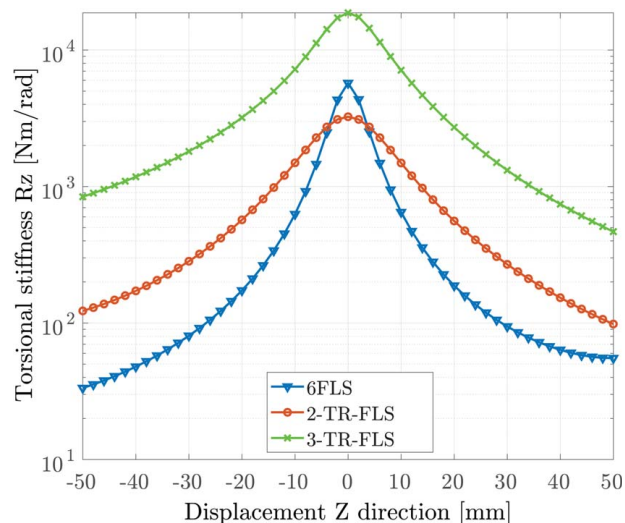
Fig. 11 Torsional stiffness around the motion axis versus displacement, of the three optimized designs

Table 3 Minimum support stiffness throughout the range of motion (100 mm) for each optimized design

Design	Minimum support stiffness
6-FLS (preexisting)	2840 (N/m)
2-TR-FLS	5811 (N/m)
3-TR-FLS	11620 (N/m)

Table 4 Optimized design variables with corresponding footprints (depicted in Figs. 7 and 8) for the three designs in Figs. 1, 5, and 6

Dimension	6-FLS	2-TR-FLS	3-TR-FLS
L_{ff} (mm)	150	149	150
W_{ff} (mm)	36	46	75
t_{ff} (mm)	0.2	0.2	0.2
W_t (mm)	—	41	28
t_t (mm)	—	0.2	0.2
H (mm)	22	50	49
α (rad)	0	0	0
L_{end} (mm)	37.5	39.4	63
L_Z (mm)	111	104	97
L_Y (mm)	150	150	150

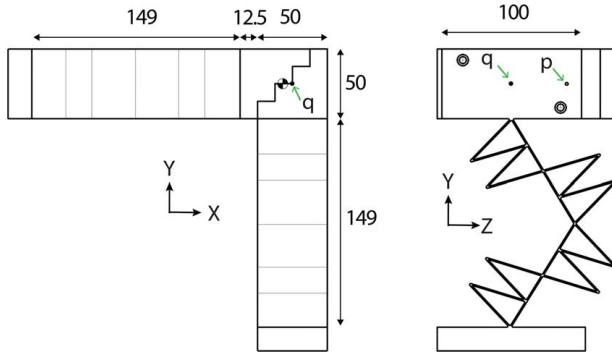Note: All designs use the maximum driving force of 10 N and maximum stress of 600 MPa.

Table 4 presents the design variables resulting from the optimizations. In all optimizations, the thickness of the flexure elements results in the lower bound of 0.2 mm. Furthermore, all designs result in the maximum driving force of 10 N, and all reach the maximum stress of 600 MPa. The height H of the flexures (approximately) reached the upper bounds of 50 mm for the 2-TR-FLS and 3-TR-FLS designs, whereas the 6-FLS design has a H value of 22 mm. The reason that the 6-FLS has a lower H value is that the stiffness in the motion direction should be low enough to satisfy the other optimization constraints: the

actuation force should not exceed the 10 Newton limit, while the end effector should reach the intended range of motion. Dimensions L_Z and L_Y are measures for the footprint of the mechanisms, as depicted in Fig. 8.
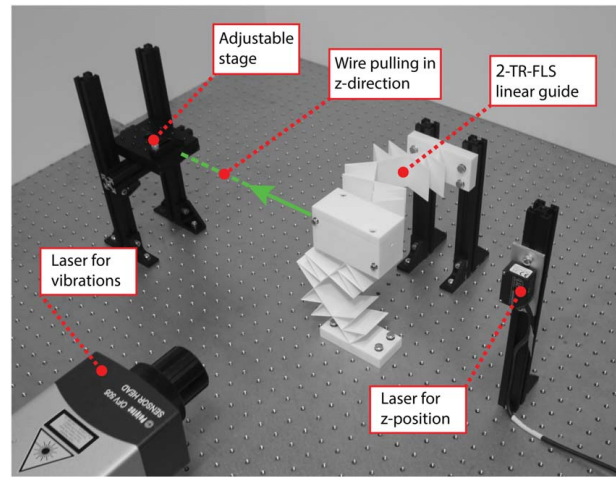
Fig. 12 Prototype of the 2-TR-FLS, dimensions in mm. Point p and q correspond to Fig. 7

Fig. 13 Experimental setup for measuring the eigenfrequencies of the 2-TR-FLS design along its range of motion

4 Experimental Validation

To validate the theoretical model, a prototype based on the optimized 2-TR-FLS design is tested experimentally. In this section, we describe the design of the prototype and the measurement setup and present the results.

4.1 Prototype. The prototype is built from Polyamide 12 (Nylon) using a selective laser sintering (SLS) process. Using Nylon instead of steel (as in the optimizations) has the advantage that the stiffness of the steel support frame can be neglected and therefore does not need to be modeled. Material properties of printed Nylon using the SLS process are experimentally tested in Ref. [32]. Taking the printing direction into account, the authors report a Young's modulus of 1.62 GPa and a Poisson ratio of 0.387. Figure 12 shows the design of the prototype. The two TR-FLS elements forming the 2-TR-FLS linear guide are printed separately and then joined using four bolts. The printing direction for each TR-FLS is in the direction perpendicular to the drawing plane of Fig. 7. Both TR-FLS elements of the prototype in Fig. 12 have staircase-shaped end effectors that fit on to each other. Some dimensions of the optimized design are changed in the prototype. Figure 12 shows that the end effector of the horizontal TR-FLS is elongated by 12.5 mm. This is to avoid collisions of the triangular segments with the other TR-FLS element. As a result W_{end} of the top TR-FLS is changed from 25 mm to 37.5 mm and that the center of mass of the end effector is shifted. The new center of mass is located 6.25 mm in negative x-direction from point q, as indicated in Fig. 12. Furthermore, the triangular segments closest to the attachment points of the TR-FLS elements in Fig. 12 are at the left side of the main leaf spring, whereas these were positioned at the right side in the optimization result. Finally, the thickness of the flexures t_t and t_{ff} (see Fig. 7) is set to 1 mm because of the changed material properties and limitations of the SLS manufacturing process. The thickness of the leaf springs and torsion reinforcements are measured at 14 positions using a micrometer with a force restrictor. The average value is used in the SPACAR model. The dimensions L_{ff} (see Fig. 7) and height H of the additively manufactured prototype is checked using a caliper. Sharp corners are rounded off with 1 mm radius fillets to avoid stress concentrations.

4.2 Measurement Setup. The support stiffness of the linear guide is validated indirectly by measuring the eigenfrequencies of the prototype. This way, inaccuracies due to stress relaxation are mitigated. The lowest eigenfrequency of the unactuated stage should have a mode shape in which the end effector moves in its intended motion direction. This frequency is ideally low, indicating a low motion stiffness. The mode shapes in the undesired directions are considered parasitic and ideally occur at high frequencies, indicating a high support stiffness.

The mass and inertia of the end effector are calculated using the CAD software SOLIDWORKS. These values are used in the SPACAR model to perform the dynamic analysis. To check the CAD software and the manufacturing process, two tests are carried out. First, the density value used in the CAD software is checked. The mass of a single TR-FLS arm is calculated using the CAD software. The printed TR-FLS arm will then be weighed and compared. As a second test, the three rotational moments of inertia I_{xx}, I_y, and I_z are checked analytically. For this, we assume that the end effector forms a rectangular block of homogeneous density with the outer dimensions depicted in Fig. 12. The inertia can then be calculated, for example, around the X-axis [26]:

$$I_x = \frac{m(a^2 + b^2)}{12} + mc^2 \qquad (6)$$

where a and b are the dimensions of the end effector in the directions Y and Z, respectively, and c is the distance from the center of mass to the point where the inertia is to be calculated, perpendicular to the chosen axis. Likewise, inertias I_y and I_z can be calculated. To estimate the mass in Eq. (6), the volume of a solid block with the outer dimensions of the end effector in Fig. 12 is calculated and the mass is calculated using the previously validated value for the density. The nuts and bolts are weighed and added to this mass. The inertia is calculated around point p in Fig. 12, which is also the point of actuation.

Figure 13 shows the measurement setup, built on a vibration isolation table. The prototype is driven (actuated) by a thin wire, which is pulled in the Z-direction using the depicted adjustable stage. The z-position is measured using a triangulation laser sensor (optoNCDT 1420). At 11 different z-positions (between every 10 mm of the displacement range), an impulse is applied at different places on the prototype using an impact hammer. The parasitic eigenfrequencies are measured using a laser Doppler sensor (Polytec OFV505) aimed perpendicular to the Z-direction. The velocity–time signal is read out by its controller unit (OFV2200), without using the filtering options. This analog signal is converted to digital using a NI USB-6008 DAQ device. The same device is used to readout the triangulation sensor, ensuring that both data sets have the same time stamp, independently from the processing speed of the laptop, which is used to read out this digital signal. The velocity–time signal is analyzed in the frequency domain using the fast-Fourier transform function in the software package MATLAB. From the resulting graphs, the eigenfrequencies on the z-positions can be read out by examining their peaks. The eigenfrequency in the motion direction is measured by removing the wire and using the laser sensor in Z-direction. Because the frequencies
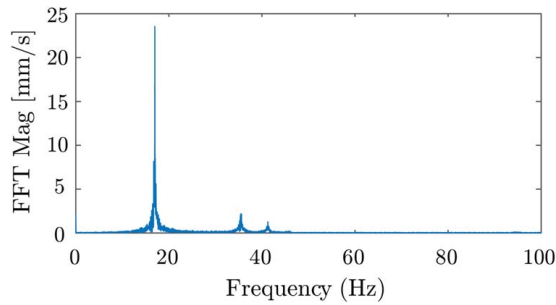
Fig. 14 Parasitic eigenfrequencies of the Nylon prototype when the end effector is at +50 mm displacement in the z-direction

are low in this direction, the sample frequency of the triangulation laser suffices. To avoid that modes are not measured, the impulses using the impact hammer are applied at different positions on the end effector and on the rest of the setup. For the same reason, the laser measuring the vibrations are pointed at different positions and angles on the end effector.

4.3 Experimental Results. Figure 14 shows the experimentally measured parasitic eigenfrequencies of the Nylon prototype when the end effector is positioned at $z = +50$ mm. Note that higher frequencies are not measured, probably due to the damping of the Nylon. At all 11 z-positions, such a frequency spectrum is plotted and the three lowest frequencies are read out. These are compared to the theoretical data, shown in Fig. 15. Each line represents the frequency of a different mode shape, computed with the SPACAR model. The line with lowest values is called the first parasitic mode shape. The black dots represent the experimental data. The eigenfrequency in motion direction at $z = 0$ is 2.1 Hz, as measured with the triangulation sensor. The raw data for all frequency plots, the postprocessing script, and the SPACAR model will be published in the *Journal of Mechanisms and Robotics*.

To quantify how well the measurements correspond to the SPACAR model, a normalized mean absolute error (NMAE) is computed for each of the three measured mode shapes. The NMAE is a regular mean absolute error normalized by the maximum value in the displacement range as follows:

$$\text{NMAE} = \frac{\frac{1}{N} \sum_{n=1}^{N} |\hat{y}_n - y_n|}{max|y|} \qquad (7)$$

where N is the amount of measured data points (11 per mode shape), $\hat{y}$ is the measured data, and y is the SPACAR model data. For the first,
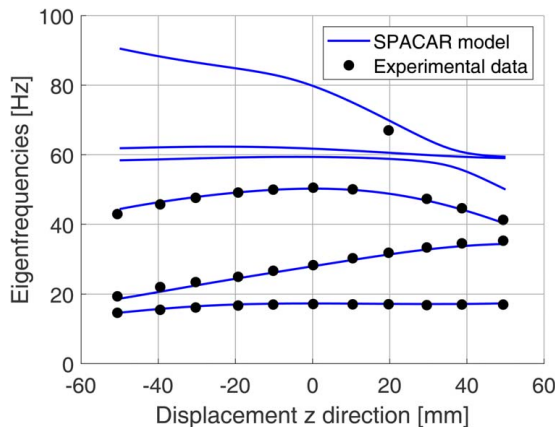
Fig. 15 Measured and modelled parasitic eigenfrequencies of the Nylon prototype of the 2-TR-FLS design. The eigenfrequency in motion direction (not displayed) is 2.1 Hz.

second, and third parasitic mode shapes, the NMAE is 1.3%, 2.0%, and 4.3%, respectively. Note the outlier in the third mode shape at $z = 20$ mm, as shown in Fig. 15. This outlier is included in the NMAE of the third mode shape and causes the higher resulting value.

The eigenfrequencies in Fig. 15 are calculated using the SPACAR software, which in turn uses mass and inertia values at point p of the end effector, calculated by the CAD software SOLIDWORKS. The density value used in the CAD software is checked by weighing a single TR-FLS arm. This results in a value of 0.280 kg, whereas the CAD software predicts 0.282 kg. This is an error of 0.71%. The inertia values calculated with the CAD model for I_x, I_y, and I_z are 8.56×10^{-4} kgm^2, 9.01×10^{-4} kgm^2, and 1.83×10^{-4} kgm^2, respectively. To check these values, first the nuts, bolts, and washers connecting the end effector are weighed, resulting in a value of 20.2×10^{-3} kg. The hand calculation of the Nylon part of the end effector results in 0.297 kg. The total of these masses is 0.317 kg, which is used to approximately calculate the inertia values, using Eq. (6). This results a I_x, I_y, and I_z of 8.22×10^{-4} kgm^2, 8.72×10^{-4} kgm^2, and 1.82×10^{-4} kgm^2, respectively. These values correspond within 5% to the values calculated by the CAD software.

The thickness t_t and t_{ff} measured with a micrometer at 14 positions are 0.99 mm on average, with a maximum deviation of 9 μm. The dimensions L_{ff} and H are checked using a caliper, resulting in the expected values of 149 and 40 mm, respectively.

5 Discussion

The 2-TR-FLS design has a smaller and less obstructive build volume than the 6-FLS, yet it outperforms the 6-FLS on the support stiffness metric in Table 3. The 3-TR-FLS design occupies a build volume similar to that of the 6-FLS, but scores four times higher on the support stiffness metric.

The experimental test of the Nylon prototype shown in Fig. 15 validates the SPACAR model. There is one outlier in the graph. This measured value could correspond to one of the higher mode shapes. The rest of the data shows good correspondence, as shown in Fig. 15. The printing process showed to be very precise according to the measurements on density and flexure thickness in Sec. 4.3. This could explain the good correspondence between experiment and model.

Figures 9 and 10 show that the support stiffness of the 6-FLS design increases at large displacements, which is unexpected. The simulations show that at the point of the support stiffness increase, the material coordinate at the fold line starts moving in the direction opposite to the motion direction (the FLS appears to be "stretched"). This might explain the support stiffness increase, either because of the decrease in curvature in the leaf springs or because the increase in motion stiffness, which also has a component in the constraining directions.

All designs in this article have a range comparable to their footprint. This is large compared to existing literature, in which a fraction of the footprint is common. All other properties of the mechanism, such as maximum stress and flexure thickness, are kept in a practically feasible range considering wire electrical discharge machining of steel, albeit at the upper limit of what is currently possible. Often in industry, shot peening is used to increase the fatigue life of flexures. This postprocessing technique cannot directly be applied when torsion reinforcement structures are present.

An additional advantage of both the new designs and the 6-FLS design is that inaccuracies in the thickness of the flexures have less impact on the motion path, compared to a planar parallelogram design. The TR-FLS element in Fig. 3 will constrain the indicated directions, regardless of the motion path of the flexures in the XY-plane. This is different from the parallelogram design, in which the in-plane axial constraints of the flexures are necessary to provide linear motion. An inaccuracy in the flexure thickness will affect their motion path, directly affecting the motion of the end effector.

Similar to most planar linear guides, the three spatial linear guides analyzed in this paper are "overconstrained" [23]. This could be a disadvantage, for example, when temperature gradients are present. The 6-FLS design has one overconstraint in rotation around the Z axis. This could, for example, be dealt with by adding a notch flexure to one of the flexure elements or by creating a torsionally compliant end effector [8]. The 2-TR-FLS linear guide has the same overconstraint, which could be removed in the same manner. Removing overconstraints in the 3-TR-FLS does not seem practical because of the large number of overconstraints.

Note that a single TR-FLS arm is not overconstrained. To understand this, a single triangle need to be observed in the TR-FLS arm in Fig. 3. This triangle consists of a main leaf spring and a torsion reinforcement structure, which in itself is a small folded leaf spring. As explained in Fig. 2 and Ref. [8], a folded leaf spring adds one constraint to a system. This single constraint is used to suppress the torsional degree-of-freedom of the main flexure. Because the different triangles in the TR-FLS arm are placed in series, no overconstraints are present in a single TR-FLS element.

The 2-TR-FLS design could be further improved. For example, more triangular elements might increase support stiffness. However, in practice, the fillets required at the attachment points of these elements will result in a large accumulations of material, increasing the stiffness in the motion direction. This will in turn increase stresses in the mechanism. A more feasible improvement would be to make the flexures tapered in the X and Y directions. The flexures would then fill up the open space in Fig. 12 (left).

6 Conclusion

In this study, a new flexure element called the TR-FLS is presented. This element is created by adding torsion reinforcement structures to a folded leaf spring, which increases its constraining directions from one to three. An advantage of this is that only two instead of five- or six-folded leaf springs are needed to create a linear guide.

A new linear guide consisting of two TR-FLS elements is presented, called the 2-TR-FLS. The design is compared to a preexisting linear guide consisting of six regular folded leaf springs (6-FLS), after optimizing both designs on a support stiffness metric. Compared to the 6-FLS design, the 2-TR-FLS design scores over twice as high on the support stiffness metric, while occupying a smaller (-33%) and less obstructive build volume.

A variation on the new linear guide is presented called the 3-TR-FLS. This linear guide is designed such that it occupies a build volume similar to that of the 6-FLS design. After optimizing this design, it scores four times higher on the support stiffness metric compared to the 6-FLS design.

A prototype of the 2-TR-FLS design is built, and the parasitic eigenfrequencies along its range of motion are measured, validating the SPACAR software used for modeling (normalized mean absolute error of 4.3%).

Conflict of Interest

There are no conflicts of interest.

Data Availability Statement

The data and information that support the findings of this article are freely available at: https://data.4tu.nl/info/en/ and https://doi.org/10.4121/16864078.v1. The authors attest that all data for this study are included in the paper.

References

[1] Howell, L. L., Magleby, S. P., and Olsen, B. M., 2013, *Handbook of Compliant Mechanisms*, John Wiley & Sons, Hoboken, NJ.
[2] Smith, S. T., 2000, *Flexures: Elements of Elastic Mechanisms*, CRC Press, Boca Raton, FL.
[3] Leach, R., and Smith, S. T., 2018, *Basics of Precision Engineering*, CRC Press, Boca Raton, FL.
[4] Cosandier, F., Henein, S., Richard, M., and Rubbert, L., 2017, *The Art of Flexure Mechanism Design*, Epfl Press, Lausanne, Switzerland.
[5] Awtar, S., and Parmar, G., 2013, "Design of a Large Range XY Nanopositioning System," ASME J. Mech. Rob., **5**(2), p. 021008.
[6] Xu, Q., 2011, "New Flexure Parallel-Kinematic Micropositioning System With Large Workspace," IEEE Trans. Rob., **28**(2), pp. 478–491.
[7] Chen, K.-S., Trumper, D., and Smith, S., 2002, "Design and Control for an Electromagnetically Driven x–y–θ Stage," Precis. Eng., **26**(4), pp. 355–369.
[8] Soemers, H., 2011, *Design Principles for Precision Mechanisms*, T-point print, Enschede, The Netherlands.
[9] Trease, B. P., Moon, Y. -M., and Kota, S., 2005, "Design of Large-Displacement Compliant Joints," ASME J. Mech. Des., **127**(4), pp. 788–798.
[10] Panas, R. M., and Hopkins, J. B., 2015, "Eliminating Underconstraint in Double Parallelogram Flexure Mechanisms," ASME J. Mech. Des., **137**(9), p. 092301.
[11] Awtar, S., Slocum, A. H., and Sevincer, E., 2007, "Characteristics of Beam-Based Flexure Modules," ASME J. Mech. Des., **129**(6), pp. 625–639.
[12] Brouwer, D. M., Otten, A., Engelen, J., Krijnen, B., and Soemers, H., 2010, "Long-Range Elastic Guidance Mechanisms for Electrostatic Comb-Drive Actuators," Proceedings of the Tenth International Conference of the European Society for Precision Engineering & Nanotechnology EUSPEN, Delft, The Netherlands, pp. 47–50.
[13] Olfatnia, M., Sood, S., Gorman, J. J., and Awtar, S., 2013, "Large Stroke Electrostatic Comb-Drive Actuators Enabled by a Novel Flexure Mechanism," J. Microelectromech. Syst., **22**(2), pp. 483–494.
[14] Hubbard, N. B., Wittwer, J. W., Kennedy, J. A., Wilcox, D. L., and Howell, L. L., 2004, "A Novel Fully Compliant Planar Linear-Motion Mechanism," ASME 2004 International Design Engineering Technical Conferences and Computers and Information in Engineering Conference, Salt Lake City, UT, American Society of Mechanical Engineers, pp. 1–5.
[15] Krijnen, B., and Brouwer, D. M., 2013, "Flexures for Large Stroke Electrostatic Actuation in MEMS," J. Micromech. Microeng., **24**(1), p. 015006.
[16] Lee, C., and Pan, R., 1997, *Cryocoolers 9*, Springer, New York, pp. 413–420.
[17] Awtar, S., and Slocum, A. H., 2005, "Flexure Systems Based on a Symmetric Diaphraghm Flexure," Proceedings of the ASPE 2005 Annual Meeting.
[18] Bos, A., 2017, "Position Actuator for the Elt Primary Mirror," PhD thesis, Eindhoven University of Technology, The Netherlands.
[19] Cacace, L., 2009, "An Optical Distance Sensor: Tilt Robust Differential Confocal Measurement with mm Range and nm Uncertainty," PhD thesis, Eindhoven University of Technology, The Netherlands.
[20] Haitjema, H., Rosielle, P., and Steijaert, H., 1997, "A Calibration Platform for Generating Parallel Displacements With Nanometre Accuracy," Proceedings of the 9th IPES-4UME, Braunschweig, Germany, pp. 456–459.
[21] Schellekens, P., Rosielle, N., Vermeulen, H., Vermeulen, M., Wetzels, S., and Pril, W., 1998, "Design for Precision: Current Status and Trends," CIRP. Ann., **47**(2), pp. 557–586.
[22] Hopkins, J. B., 2015, "A Visualization Approach for Analyzing and Synthesizing Serial Flexure Elements," J. Mech. Rob., **7**(3), p. 031011.
[23] Hale, L. C., 1999, "Principles and Techniques for Designing Precision Machines," Lawrence Livermore National Lab.(LLNL), Livermore, CA, Technical Report.
[24] Hopkins, J. B., and Culpepper, M. L., 2010, "Synthesis of Multi-Degree of Freedom, Parallel Flexure System Concepts via Freedom and Constraint Topology (Fact)—Part I: Principles," Precis. Eng., **34**(2), pp. 259–270.
[25] Ugural, A. C., and Fenster, S. K., 2003, *Advanced Strength and Applied Elasticity*, Prentice Hall PTR, Hoboken, NJ.
[26] Hibbeler, R., 2005, *Mechanics of Materials*, Prentice Hall, Hoboken, NJ.
[27] Wiersma, D., Boer, S., Aarts, R., and Brouwer, D., 2014, "Design and Performance Optimization of Large Stroke Spatial Flexures," ASME J. Comput. Nonlinear. Dyn., **9**(1), p. 011016.
[28] Naves, M., Brouwer, D., and Aarts, R., 2017, "Building Block-Based Spatial Topology Synthesis Method for Large-Stroke Flexure Hinges," ASME J. Mech. Rob., **9**(4), p. 041006.
[29] Bernardoni, P., Bidaud, P., Bidard, C., and Gosselin, F., 2004, "A New Compliant Mechanism Design Methodology Based on Flexible Building Blocks," SPIE, San Diego, CA, pp. 244–254.
[30] Jonker, J., and Meijaard, J., 1990, *SPACAR — Computer Program for Dynamic Analysis of Flexible Spatial Mechanisms and Manipulators*, Springer, Berlin/ Heidelberg.
[31] Nelder, J. A., and Mead, R., 1965, "A Simplex Method for Function Minimization," Comput. J., **7**(4), pp. 308–313.
[32] Faes, M., Wang, Y., Lava, P., and Moens, D., 2015, "Variability in the Mechanical Properties of Laser Sintered PA-12 Components," Proceedings of the 26th Annual International Solid Freeform Fabrication Symposium, Austin, TX, pp. 847–856.